JGR Oceans

RESEARCH ARTICLE
10.1029/2020JC016479

Widespread Mesoscale Dipoles in the Global Ocean

Qinbiao Ni[1,2,3], Xiaoming Zhai[3], Guihua Wang[4], and Chris W. Hughes[5]

[1]State Key Laboratory of Satellite Ocean Environment Dynamics, Second Institute of Oceanography, Ministry of Natural Resources, Hangzhou, China, [2]College of Ocean and Earth Sciences, Xiamen University, Xiamen, China, [3]Centre for Ocean and Atmospheric Sciences, School of Environmental Sciences, University of East Anglia, Norwich, UK, [4]Department of Atmospheric and Oceanic Sciences and Institute of Atmospheric Sciences, Fudan University, Shanghai, China, [5]School of Environmental Sciences, University of Liverpool and National Oceanography Centre, Liverpool, UK

Abstract Mesoscale eddies are ubiquitous and energetic features in the ocean. Although eddies are known to form dipoles from time to time, it is unclear how often they do so. Using satellite altimetry data, here we show that mesoscale dipoles are surprisingly widespread in the global ocean. About 30–40% of the mesoscale eddies identified in altimeter data are paired up as dipoles, and the percentage is even higher in energetic regions such as the Gulf Stream and the Southern Ocean. Composite analysis involving Argo float data further reveals that these mesoscale dipoles have a relatively uniform three-dimensional structure. We find that the presence of mesoscale dipoles can strongly enhance wind Ekman pumping velocity and lead to deep-reaching vertical motions inside the dipoles via eddy deformation and frontogenesis. Such strong vertical exchanges promoted by mesoscale dipoles may play an important role in regulating the Earth's biogeochemical processes.

Key Points:
- Mesoscale dipoles are widespread features in the global ocean
- Mesoscale dipoles have a relatively uniform three-dimensional structure
- Mesoscale dipoles can potentially lead to strong vertical exchanges in the ocean

Correspondence to:
X. Zhai and G. Wang,
xiaoming.zhai@uea.ac.uk;
wanggh@fudan.edu.cn

Citation:
Ni, Q., Zhai, X., Wang, G., & Hughes, C. W. (2020). Widespread mesoscale dipoles in the global ocean. *Journal of Geophysical Research: Oceans*, *125*, e2020JC016479. https://doi.org/10.1029/2020JC016479

Received 29 JUN 2020
Accepted 5 OCT 2020
Accepted article online 7 OCT 2020

1. Introduction

Mesoscale eddies, accounting for the majority of the ocean's kinetic energy, play a vital role in transporting climatically important properties and tracers such as momentum, heat, carbon, and nutrients (Conway et al., 2018; Dong et al., 2014; Wunsch, 1999; Zhang et al., 2014). Significant progress has been made over the last few decades in characterizing the global distribution of the eddy field and in understanding its dynamics and energetics (Chelton et al., 2011; Nikurashin et al., 2013; Xu et al., 2016; Zhai et al., 2010). Ocean eddies are known to frequently interact with each other and can sometimes form dipoles that consist of two coupled counterrotating eddies separated by a central jet between them (Flierl et al., 1983; Pallàs-Sanz & Viúdez, 2007; Pidcock et al., 2013). In fact, theory predicts that mesoscale dipoles are the simplest dynamically consistent, and potentially ubiquitous, features in the ocean (Flierl et al., 1983). Mesoscale eddy dipoles have indeed been observed a number of times near the eastern boundary (Ahlnäs et al., 1987; Callendar et al., 2011; Pidcock et al., 2013; Simpson & Lynn, 1990) and also in association with the western boundary currents (de Ruijter et al., 2004; Hooker et al., 1995). Most recently, via visual analysis, nine rapidly moving eddy dipoles were identified in satellite altimeter data in the midlatitude ocean to the north of the Antarctic Circumpolar Current (Hughes & Miller, 2017). However, due to the sporadic nature of past observations, mesoscale dipoles are often regarded as a feature of curiosity, and it is not clear how abundant these eddy dipoles are in the world ocean. Furthermore, studies relying on satellite altimeter data alone provide no information about the vertical structure of the dipoles (Hughes & Miller, 2017). Therefore, the distribution and three-dimensional (3-D) structure of mesoscale dipoles remain unknown, especially on the global scale.

Knowledge of the number and structure of mesoscale dipoles, on the other hand, may prove important for understanding lateral and vertical exchanges of fluid and tracers in the ocean and as such important for understanding the Earth's biogeochemical tracer budgets. For example, mesoscale eddies tend to propagate westward at speeds close to the speeds of long baroclinic Rossby waves (Chelton et al., 2011). An exception to this behavior is when eddies pair up and form dipoles, which then enables them to travel at speeds potentially larger than the Rossby wave speed, to the east as well as west, leading to unusual lateral transports of heat, carbon, and nutrients (Hughes & Miller, 2017). The presence of mesoscale dipoles may also impact eddy-wind interactions (Gaube et al., 2015; McGillicuddy et al., 2007; Zhai & Greatbatch, 2007) and promote vertical motions in the upper ocean, in addition to those induced by isolated eddies, via eddy deformation and frontogenesis (Hoskins et al., 1978; Klein & Lapeyre, 2009; Martin & Richards, 2001). Such vertical

motions are vital for supplying nutrients to the euphotic zone to support primary productivity and for sequestering carbon to the deep ocean.

The goal of this study is to investigate the distribution, 3-D structure, and impact of mesoscale dipoles in the global ocean using satellite and Argo float data together with a simple automatic dipole identification and tracking algorithm. The paper is organized as follows. In section 2, we describe the data and methods used and an automatic mesoscale dipole identification and tracking algorithm developed in this study. In section 3, we present and discuss the global dipole distribution, the 3-D dipole structure, and dipole-induced vertical motions. Finally, conclusions are provided in section 4.

2. Data and Methods

2.1. Data Processing

The altimeter-derived daily maps of sea level anomalies (SLAs) provided by Copernicus Marine Environment Monitoring Service on a 0.25° × 0.25° grid are used in this study for the period from January 1998 to December 2017. Following previous studies (e.g., Xu et al., 2016), each daily SLA map is high pass-filtered using a Gaussian filter function with a half-power cutoff wavelength of 10° to remove large-scale SLA signals associated with the wind forcing and surface heating/cooling before we apply the eddy identification procedure.

The Argo float data are obtained from the China Argo Real-time Data Center for the same 20-year period. A total of 937,806 quality-controlled temperature and salinity profiles are selected for this study. All these profiles have measurements at depths shallower than 10 m and deeper than 1,500 m. For each Argo profile, potential density ρ is derived from the temperature and salinity measurements and then linearly interpolated in the depth range of 10–1,500 m at an interval of 10 m. Mesoscale potential density anomalies (ρ') are obtained by subtracting from each Argo profile a local climatological mean profile. The climatological mean profile is computed by averaging all the Argo profiles within an area of 5° × 5° (and within 45 days) centered at the profile under consideration. The subsurface pressure anomalies are then calculated by integrating the hydrostatic equation downward from the sea surface (Mulet et al., 2012):

$$P' = \rho_{top} g \eta_A + \int_z^0 \rho' g dz,$$

where ρ_{top} is the density at the shallowest measurement of the Argo profile, g is gravity, and η_A is the SLA at the location of the Argo profile.

The global daily microwave sea surface temperature (SST) data provided by the Remote Sensing Systems and daily QuikSCAT scatterometer wind stress and vector wind data provided by IFREMER are used from 2000 to 2009 to investigate the effect of mesoscale dipoles on surface wind stress and wind Ekman pumping. Both data sets are provided on a 1/4° × 1/4° grid. To remove large-scale signals unrelated to mesoscale air-sea interactions, the SST and wind stress data are spatially high pass-filtered with a half-power cutoff wavelength of 6° before we apply composite analysis (Gaube et al., 2015).

2.2. Eddy and Dipole Identification

Our eddy identification method is based on the SLA geometry following a previous algorithm (Chaigneau et al., 2011; Chelton et al., 2011). Contours are first extracted from high pass-filtered SLA maps at an interval of 1 cm (Chelton et al., 2011). The center of an eddy is defined as the average position of the innermost closed SLA contour, and the edge of the eddy is defined as the outermost closed SLA contour that encloses no more than one eddy center. The amplitude of the eddy is then taken to be the SLA difference between the eddy center and its edge. Given the accuracy of satellite altimetry measurements, only eddies with amplitude larger than 2 cm are included in this study (Chaigneau et al., 2011).

There is no clear definition of mesoscale dipoles in the literature. Here we apply two simple, yet physically motivated, criteria to distinguish the dipoles from the more isolated nondipole eddies. First, the distance between the two counterrotating eddy centers should be shorter than the sum of their radii. This criterion ensures there is eddy deformation and disqualifies Eddies A1 and C1 in Figure 1a as a dipole. Second, there should be only one velocity extremum between the two eddy centers. This strict criterion makes sure that the

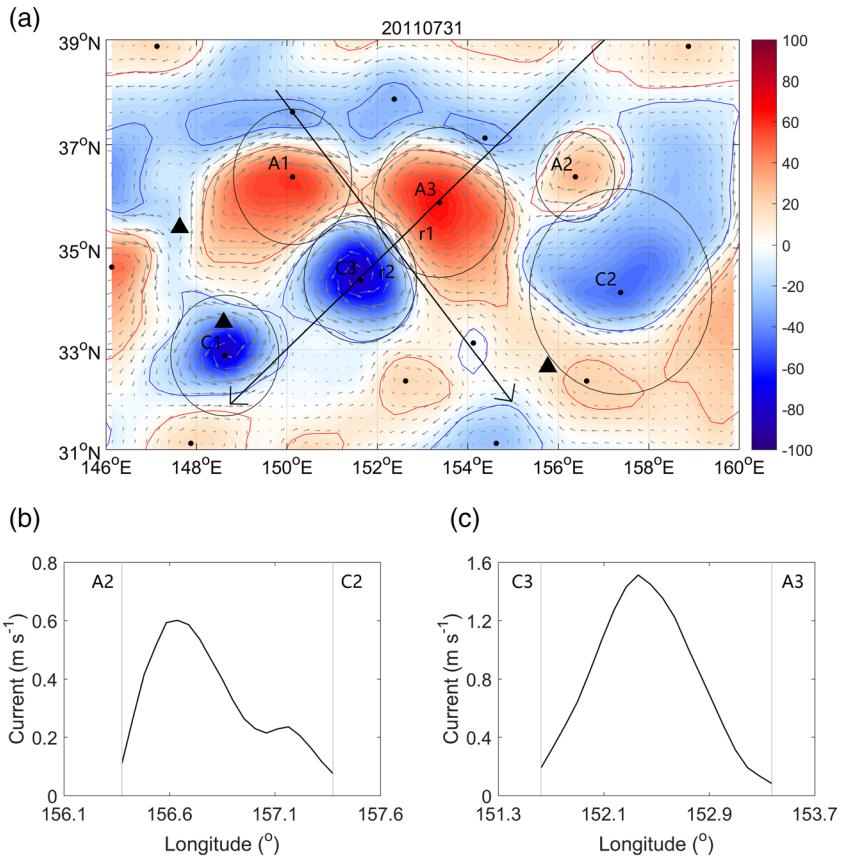

Figure 1. Identification of mesoscale ocean dipoles from altimeter data. (a) A snapshot of SLA (cm) in the Kuroshio Extension (KE) region on 31 July 2011. Gray arrows indicate surface geostrophic currents, red (blue) closed contours mark the edges of anticyclonic (cyclonic) eddies, black circles are circles that have the same area as the eddies, and black dots and triangles mark the eddy centers and the locations of Argo profiles, respectively. Long black crossed arrows represent a dipole coordinate system, in which the coordinate center or dipole center is chosen to be the location of the velocity maximum between the eddy pair, the negative (positive) x axis is toward the center of the anticyclonic (cyclonic) eddy, and r_1 (r_2) is the distance from the dipole center to the center of the anticyclonic (cyclonic) eddy. (b) Geostrophic currents (m s^{-1}) between the anticyclonic and cyclonic eddy pair A2-C2. (c) The same with Figure 1b but for the eddy pair A3-C3.

two eddies are tightly coupled and disqualifies Eddies A2 and C2 as a dipole since there are two velocity maxima between their eddy centers (Figure 1b). On this snapshot of SLA, both eddy pairs A3-C3 and A1-C3 are qualified to be dipoles (Figures 1a and 1c). In the situation where multiple eddies are tightly coupled, each pair of eddies that satisfy the dipole detection criteria is regarded as a dipole. The criteria used here enable automatic detection of mesoscale dipoles in the global ocean over the 20-year study period, which is not possible relying on visual inspection (Hughes & Miller, 2017). We have conducted additional tests and found that the results are not overly sensitive to adjustments of the criteria.

2.3. Eddy and Dipole Tracking

Dipoles are tracked by finding the smallest dissimilarity parameter (Penven et al., 2005; Souza et al., 2011) from time step i to time step $i + 1$ within a search circle centered at the dipole center at time step i:

$$\Delta = \sqrt{\left(\frac{R_1^i - R_1^{i+1}}{R_1^i}\right)^2 + \left(\frac{\eta_1^i - \eta_1^{i+1}}{\eta_1^i}\right)^2 + \left(\frac{R_2^i - R_2^{i+1}}{R_2^i}\right)^2 + \left(\frac{\eta_2^i - \eta_2^{i+1}}{\eta_2^i}\right)^2},$$

where Δ is the dissimilarity parameter, R_1 (R_2) is the radius of the anticyclonic (cyclonic) eddy of the dipole identified, and η_1 (η_2) is the SLA at the center of the anticyclonic (cyclonic) eddy. For isolated

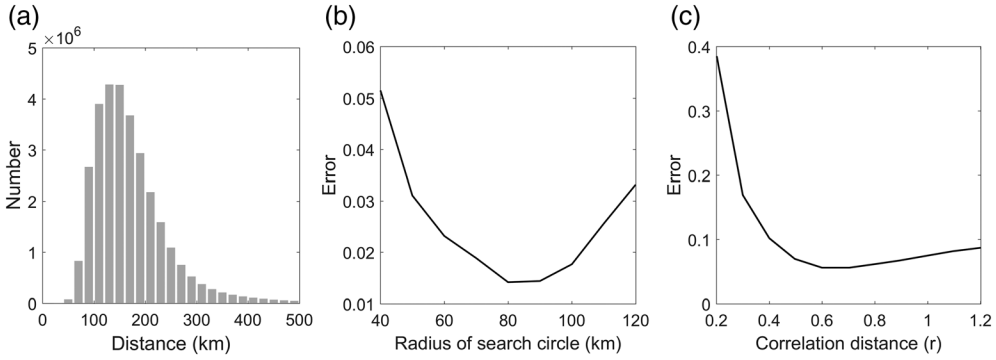

Figure 2. (a) Histogram of distance (km) between adjacent eddy centers. (b) Tracking error as a function of search circle radius. (c) Error of the objective analysis as a function of correlation distance.

eddies, only the first (last) two terms in the equation of dissimilarity parameter are kept to track anticyclonic (cyclonic) eddy centers. Dipole (eddy) tracking automatically terminates when dipole (eddy) is no longer found within the search circle. Given that the distance between two eddy centers identified from altimeter data is typically larger than 80 km and that no eddies travel longer than 80 km in 1 day, the radius of the search circle (rs) is set to be 80 km, which yields the smallest tracking error (Figures 2a and 2b) of

$$er = \frac{|F(rs_i) - F(rs_{i-1})| + |F(rs_i) - F(rs_{i+1})|}{2|F(rs_i)|},$$

where er is the error, $F(rs)$ is the field of eddy propagation speed using an array of rs with an increment of 10 km, i is the index of the rs array, and double vertical lines denote the norm. An alternative tracking method of finding the closest centroid of the outermost closed SLA contour (Chelton et al., 2011) yields very similar results (not shown).

2.4. Dipole Composite

The surface dipole composite analysis is based on altimeter data. We first set a dipole coordinate system, where the coordinate center or dipole center is defined as the location of the velocity maximum of the jet between the eddy pair, with the centers of anticyclonic and cyclonic eddies on the negative and positive x axis, respectively, in both hemispheres (Figure 1a). Defining the distance from the dipole center to the center of the anticyclonic eddy as r_1 and to the center of the cyclonic eddy as r_2, we create a dipole-centric coordinate for composite analysis with a resolution of 0.1 (r_1) × 0.1 (r_1) for the anticyclonic eddy and 0.1 (r_2) × 0.1 (r_2) for the cyclonic eddy. The surface dipole structure is then obtained by averaging surface pressure anomalies ($P' = \rho_0 g\eta$) in the dipole coordinate, where ρ_0 is the reference density and η is the SLA interpolated onto the dipole grid.

Argo float data are used for subsurface composite analysis of the dipoles. First, the locations of Argo profiles inside and close to the detected dipoles are transformed onto the dipole coordinate system. Then the subsurface ρ' and P' at Argo locations at the same depth level are objectively interpolated onto the 0.1 × 0.1 dipole grid and composite averaged. The spatial correlation distance d used for objective interpolation is decided by $F(d)$ beforehand, in a way similar to how the tracking error is estimated in section 2.3, where $F(d)$ is the field from objective analysis using an array of d with an increment of 0.1. The optimal d is chosen to be 0.6 since it gives the smallest error (Figure 2c).

3. Results

3.1. Global Dipole Distribution

Our analysis starts with the identification of over 29 million snapshots of mesoscale ocean eddies from daily maps of satellite-derived SLA over a period of 20 years (January 1998 to December 2017). The eddies are detected based on closed contours of SLA (Chaigneau et al., 2011; Chelton et al., 2011). We then apply the

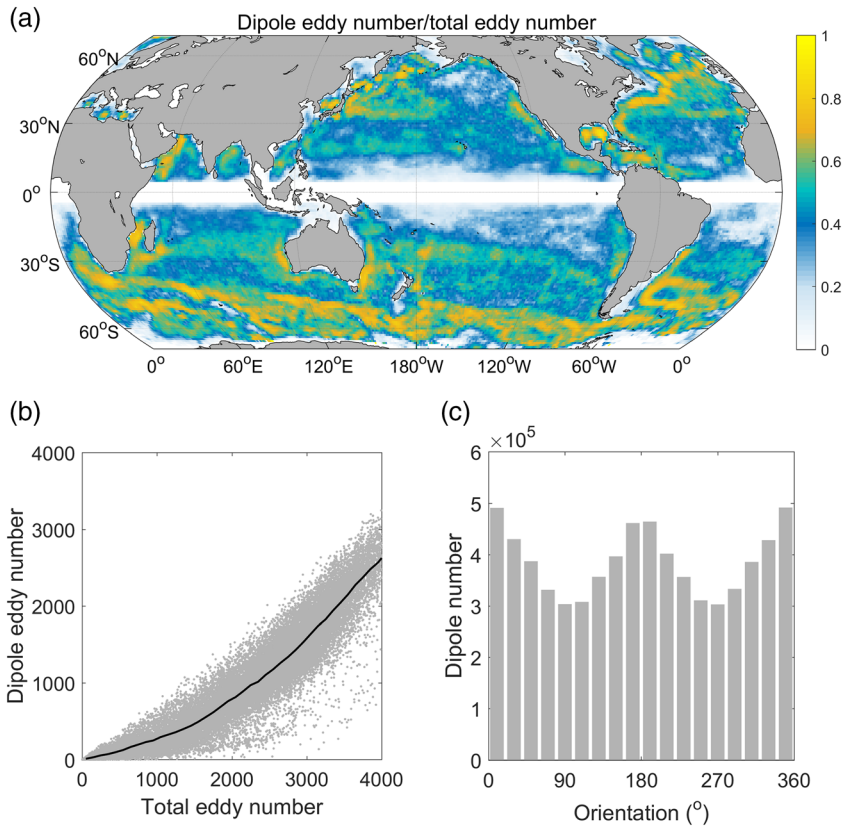

Figure 3. Global distribution of mesoscale ocean dipoles. (a) Ratio of the number of dipole eddies to the number of total eddies on a 1° × 1° grid. Dipole eddy (total eddy) number here refers to the number of times a grid point is found to be inside of a detected dipole (eddy) within the 20-year period. (b) Scatter diagram (gray dots) of the dipole eddy number versus total eddy number on each grid point. Black curve denotes its mean value. (c) Histogram of dipole orientation. The orientation in degrees measures the position of the anticlockwise-rotating eddy relative to the clockwise-rotating eddy. For example, 0° or 360° (180°) means that the anticlockwise-rotating eddy is located to the north (south) of the clockwise-rotating eddy.

two simple, yet physically motivated, kinematic criteria to distinguish eddy dipoles from the rest of more isolated nondipole eddies. Overall, about 12 million snapshots of dipole eddies are identified globally over the 20-year period, which means that close to 40% of the eddies detected from altimeter SLA maps are paired up as dipoles. The surprisingly large numbers of mesoscale dipoles found in this study corroborate a previous theoretical prediction that dipoles are dynamically natural and widespread features in turbulent geophysical fluids such as the ocean (Flierl et al., 1983). As one would expect, dipoles occur much more frequently in the western boundary current regions and also in the Antarctic Circumpolar Current region where the eddies are known to be more energetic and more tightly grouped (Figure 3a). Indeed, the number of dipoles found in each location is generally proportional to the number of eddies found there (Figure 3b). Although the dipoles can exist at any orientation and their orientation can vary over their lifetime, there is a preference for the dipole eddies to be aligned in the meridional direction (Figure 3c). This preferred north-south orientation is consistent with the fact that, on a sphere, steady propagation of isolated mesoscale dipoles is only possible in a zonal direction (Hughes & Miller, 2017; Nycander, 1992).

The gridded altimetry data have a resolution of 0.25° × 0.25° and are subject to filtering process and objective interpolation (Pujol et al., 2016), which smooth out some velocity extrema and may introduce spurious SLA dipole patterns (especially near the coasts) and as a result overestimate the number of mesoscale dipoles that satisfy our dipole detection criteria. On the other hand, because of the resolution of altimetry data, some mesoscale features are likely to be underestimated or even completely missed, particularly at high

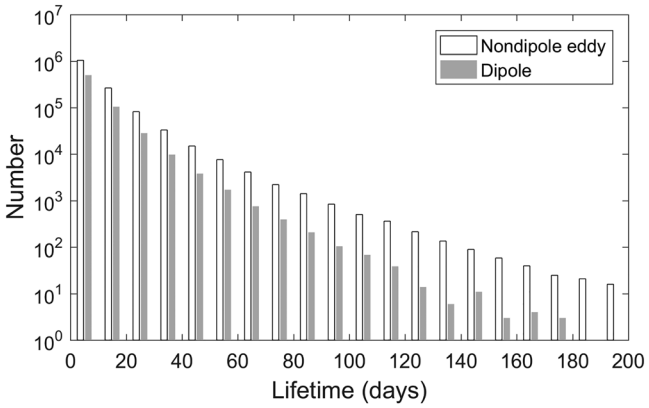

Figure 4. Histogram of the lifetimes of nondipole eddies and dipoles in the global ocean over the 20-year study period.

latitudes where the radii of deformation are small. Here we use the daily SLA output from the (1/12th)° HYCOM simulation to provide an estimate of errors potentially induced by the limited spatial resolution of altimeter data. First, the HYCOM SLA output is subsampled from the original 0.08° × 0.08° model grid to a coarser grid of 0.25° × 0.25° and high pass-filtered to remove the large-scale signals. Then, mesoscale eddies and dipoles are identified based on SLA contours on the coarser 0.25° × 0.25° grid. Globally, about 35% of the eddies identified in the subsampled HYCOM SLA output are paired up as dipoles according to our dipole detection criteria, slightly lower than the 40% found in altimeter data. We then extract contours of SLA from the original 0.08° × 0.08° model grid and plot them between dipole centers identified on the coarser 0.25° × 0.25° grid. It is found that about 75% of the dipoles identified on the 0.25° × 0.25° grid remain as dipoles. In other words, subsampling to the coarser grid has resulted in a 25% overestimate of the number of mesoscale dipoles. Taking this potential error into account, we suggest that between 30% and 40% of the eddies detected in satellite altimeter data are coupled as dipoles. Note that neither the altimetry data nor HYCOM model resolve submesoscale eddies or dipoles.

To see how long mesoscale dipoles typically last, we analyze the lifetime of dipoles identified and tracked over the 20-year study period. The average lifetime of dipoles (~8.5 days) is found to be slightly shorter than that of nondipole eddies (~10 days), although some dipole eddy pairs can be tracked for as long as over half a year (Figure 4). It is worth pointing out that although the gridded altimetry product used in this study has a daily resolution, it is unlikely a true 1-day sampling of the sea level due to the mixture of 10- and 35-day repeating satellite ground tracks and the optimal interpolation method used. While the altimetry data may allow close to a daily sampling over eddy scales at high latitudes, this is not true at low latitudes. Careful visual inspection shows that, during their propagation, dipole eddies can break up upon the impact of other vortices or become less tightly coupled such that they no longer satisfy the two criteria used in our study for automatic dipole detection. As a consequence, comparing to the trajectories of more isolated eddies, the trajectories of dipoles tend to be on average shorter. We then use the tracked dipole trajectories to estimate dipole propagation speeds. While there are cases where eddy dipole pairs move much faster compared to the nondipole eddies as found in previous studies (Hughes & Miller, 2017), the average dipole propagation speed is found to be comparable to that of the nondipole eddies. This result further shows that while a significant fraction of mesoscale eddies are paired as dipoles at any given time, dipole pairing is intermittent and the identified dipoles often break up during subsequent evolution owing to interactions with the neighboring eddies, as found in 2-D turbulence simulations where the lifetime of dipoles is often limited by collisions with other flow structures such as isolated vortices or even a background of weak vorticity (e.g., McWilliams et al., 1981). As a result, the propagation speeds of the dipoles vary greatly, in part depending on the density of eddies nearby.

3.2. Three-Dimensional Dipole Structure

To obtain the 3-D structure of the dipoles, we first compute the sea surface pressure anomalies from the spatially high pass-filtered SLA and then composite average them in a rotated dipole-centric coordinate system/grid in which the anticyclonic eddy is oriented to the left of the cyclonic eddy in both hemispheres. Our composite analysis reveals a nearly perfectly antisymmetric dipole pattern, similar to that predicted by the theory (Flierl et al., 1980), except for the additional crescents on both flanks of the dipole (Figure 5a). The magnitude of the dipole-induced surface pressure anomaly is close to 0.15 dbar, that is, ~15 cm for the corresponding SLA anomaly. We find that the horizontal pattern of the dipole's surface pressure anomaly, after being normalized by its magnitude, is well fitted by the function $P_h^{'} = -x \cdot (1.61 - (0.26x^2 + 0.36y^2)) \cdot exp(-(0.31x^2 + 0.41y^2))$ (Figures 6a and 6b). The shape of the dipole pattern, that is, bulging in the x direction in Figure 5a, indicates that the composite dipole is nonlinear. Recall that the two eddies of a liner dipole are more compressed against each other such that the vorticity of a linear dipole is characterized by a circular envelope (Batchelor, 1967). Furthermore, the additional crescents in the surface pressure field on the flanks of the dipole indicate that the composite dipole is externally "coated". The effect of the coats, as shown by

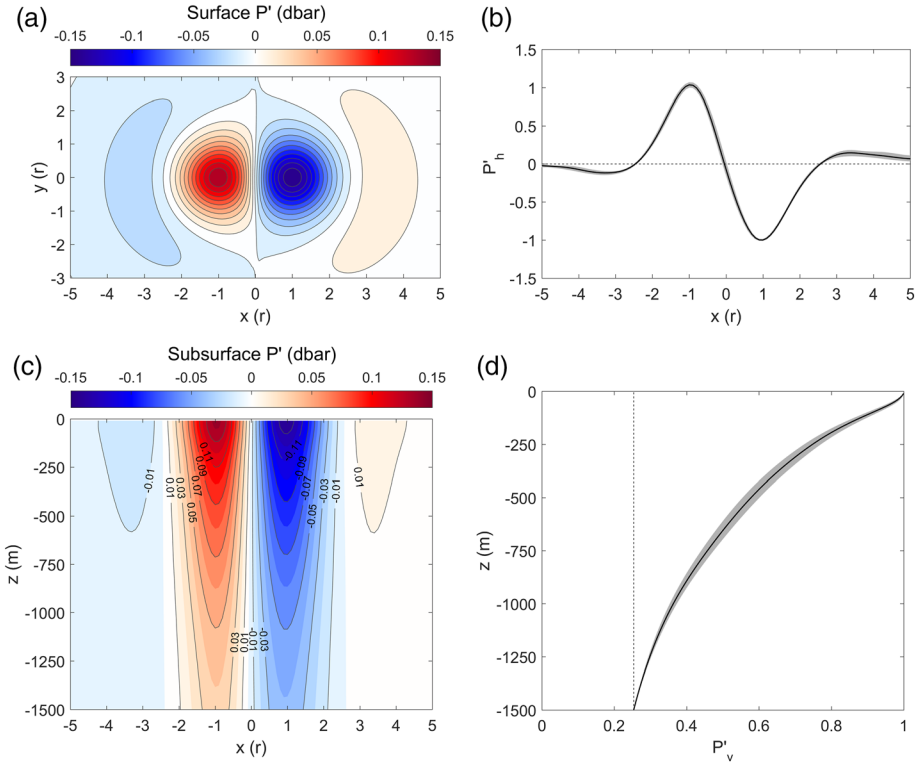

Figure 5. Three-dimensional composite structure of mesoscale dipoles. (a) Composite average of surface pressure anomalies P' (dbar) in the dipole-centric coordinate. Black contours correspond to 20 iso-contours of P' with equal intervals. (b) Horizontal component (P'_h) of P' normalized by its magnitude at each level along $y = 0$. Black curve and gray shading denote the mean and one standard deviation, respectively. (c) Vertical P' section (color shading and contours) of the composite dipole along $y = 0$. (d) The same as Figure 5b but for the vertical component (P'_v) of P' (normalized by its surface value) inside the composite dipole.

Couder and Basdevant (1986), is to initially slow down the two vortices by compressing them against each other to form a linear dipole. Indeed, when a quasi-geostrophic reduced-gravity model is initialized with the vorticity field associated with the composite dipole, it gradually evolves into a linear dipole which then translates at a much greater speed—four to five times the translation speed of the initial nonlinear dipole (Appendix A.1; Figure A1; Couder & Basdevant, 1986; Hesthaven et al., 1995; McWilliams & Zabusky, 1982). However, this is what happens when the dipole is placed in a medium that is at rest. The fact that the composite dipole derived from altimeter data takes the form of a nonlinear dipole with external coating, rather than evolving into a linear dipole, suggests again that dipole pairing in the ocean is intermittent and dipoles often become prematurely disassociated or destructed when they encounter other dipoles, isolated eddies, or even a background of weak vorticity.

To determine the vertical structure of the dipoles, 581,223 quality-controlled Argo temperature and salinity profiles located on the dipole grid over the same 20-year period are used. For each Argo profile, the subsurface pressure anomaly is obtained by integrating the hydrostatic equation downward from the sea surface using SLA and Argo density anomalies. In doing this, we avoid the need to assume a reference depth of no motion that often proves to be problematic, although further analysis shows that combining the two independently processed data sets (SLA and Argo) in the hydrostatic integration can potentially induce an error of ~10% (Appendix A.2; Figure A2). Float profiles that are located in and around the detected dipoles are then transformed onto the dipole coordinate before their pressure anomalies are composite averaged at each depth level. Interestingly, the horizontal patterns of the subsurface pressure anomalies at different depths are remarkably similar to each other (Figure 5b), while their magnitudes decay exponentially with depth (Figures 5c and 5d).

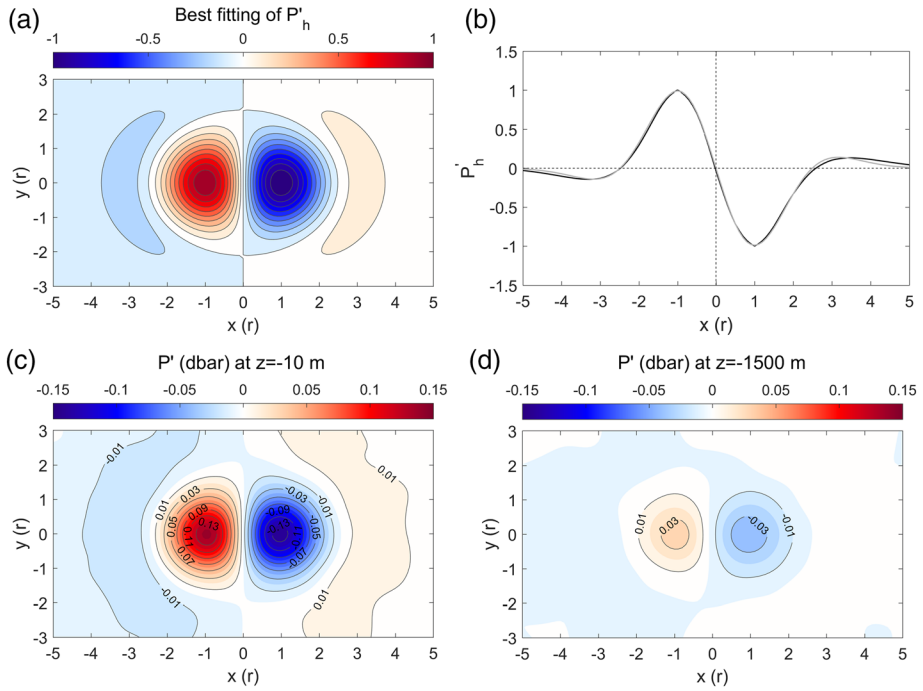

Figure 6. (a) Best fitting function for composite average of surface pressure anomalies, $P'_h = -x \cdot (1.61 - (0.26x^2 + 0.36y^2)) \cdot exp(-(0.31x^2 + 0.41y^2))$. Black contours denote 20 iso-contours of P'_h with equal intervals. (b) Composite (black) and fitted (gray) dipole-induced surface pressure anomalies along $y = 0$. (c) Horizontal pattern of the composite P' (dbar) at 10 m depth. (d) The same with Figure 6c but at 1,500 m depth.

Results from composite analysis therefore suggest that the 3-D dipole structure can be described, and potentially reconstructed, by a combination of two simple mathematical functions, that is, $P' = P'_h \cdot P'_v$, where $P_h{}'$ describes a horizontal antisymmetric pattern and $P_v{}'$ a vertical exponential attenuation profile (see Zhang et al., 2013, for an example for mesoscale eddies). We then reconstruct P' and ρ' fields associated with the composite dipole in the following way,

$$P' = P'_{bc} + P'_b$$
$$= (1-\gamma) \cdot \rho_0 g \frac{\overline{\eta_1 - \eta_2}}{2} \cdot P'_{fit} \cdot P'_v + \gamma \cdot \rho_0 g \frac{\overline{\eta_1 - \eta_2}}{2} \cdot P'_{fit},$$
$$\rho' = -\frac{1}{g}\frac{\partial P'_{bc}}{\partial z}$$

where P'_b is the dipole pressure anomaly at 1,500 m depth, P'_{bc} is pressure anomaly associated with dipole density anomalies, γ is the ratio of the value of P'_v at the surface to that at 1,500 m depth, and P'_{fit} is the best fitting function for the surface P'_h. The dipole reconstructed in this way indeed faithfully reproduces the structure (e.g., potential density and geostrophic velocity anomalies) of the composite dipole obtained based on 20 years of altimeter data and Argo profiles (Figure 7). Furthermore, the reconstructed dipole filters out small-scale perturbations existing in the dipole composite and will be used hereafter to show the impact of the mesoscale dipole structure on vertical motions in the upper ocean and also on eddy-wind interactions.

3.3. Dipole-Induced Vertical Motions

To estimate the vertical velocity associated with mesoscale dipoles as a result of eddy deformation and frontogenesis, we use the Q-vector form of the quasi-geostrophic (QG) omega equation (Hoskins et al., 1978; Klein & Lapeyre, 2009; Martin & Richards, 2001), that is,

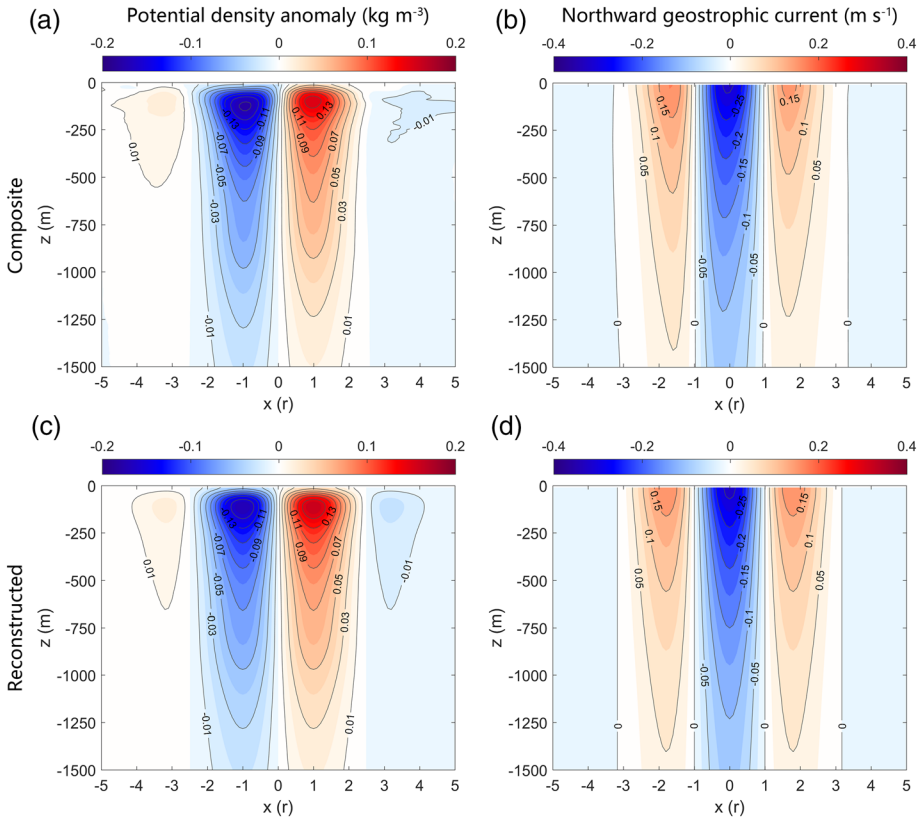

Figure 7. Comparison of composite and reconstructed dipoles. (a, b) Vertical section of potential density anomaly (kg m^{-3}) and northward geostrophic current (m s^{-1}) of the composite dipole along $y = 0$. (c, d) The same with Figures 7a and 7b but for the reconstructed dipole.

$$f_0{}^2\frac{\partial^2 w}{\partial z^2}+\left(\frac{\partial^2}{\partial x^2}+\frac{\partial^2}{\partial y^2}\right)(N^2 w)=\frac{\partial Q_x}{\partial x}+\frac{\partial Q_y}{\partial y},$$

where $N^2=-\frac{g}{\rho_0}\frac{\partial \rho}{\partial z}$ is the buoyancy frequency squared, f_0 is the Coriolis parameter, and $Q_x=2f_0\left(\frac{\partial v}{\partial x}\frac{\partial u}{\partial z}+\frac{\partial v}{\partial y}\frac{\partial v}{\partial z}\right)$ and $Q_y=-2f_0\left(\frac{\partial u}{\partial x}\frac{\partial u}{\partial z}+\frac{\partial u}{\partial y}\frac{\partial v}{\partial z}\right)$ are the x and y components of the Q vector, respectively. The dipole geostrophic velocity is calculated via geostrophic balance, with

$$u=-\frac{1}{\rho_0 f_0}\frac{\partial P'}{\partial y},\ v=\frac{1}{\rho_0 f_0}\frac{\partial P'}{\partial x}.$$

The dipole vertical velocity is then diagnosed on the 0.1 × 0.1 dipole grid with the condition of $\frac{dw}{dz}=0$ at the bottom boundary and $w = 0$ at the other boundaries.

Our calculation reveals a horizontal quadrupolar pattern of alternating upwelling and downwelling cells (Figure 8a), broadly similar to the dipole-induced vertical velocity field simulated by an idealized numerical model (Pallàs-Sanz & Viúdez, 2007). Importantly, these upwelling and downwelling cells associated with frontogenesis processes are deep reaching, extending from the surface to a depth of at least 1,500 m with maximum vertical velocities centered at about 600 m depth (Figure 8b). In contrast, there are no such ageostrophic vertical motions associated with the dipole structure in circular isolated eddies (Martin & Richards, 2001). Averaged over all the dipoles detected in the global ocean, the dipole-induced vertical velocity has a magnitude of about ±0.6 m day^{-1}, while the magnitude can increase by more than a factor of 3

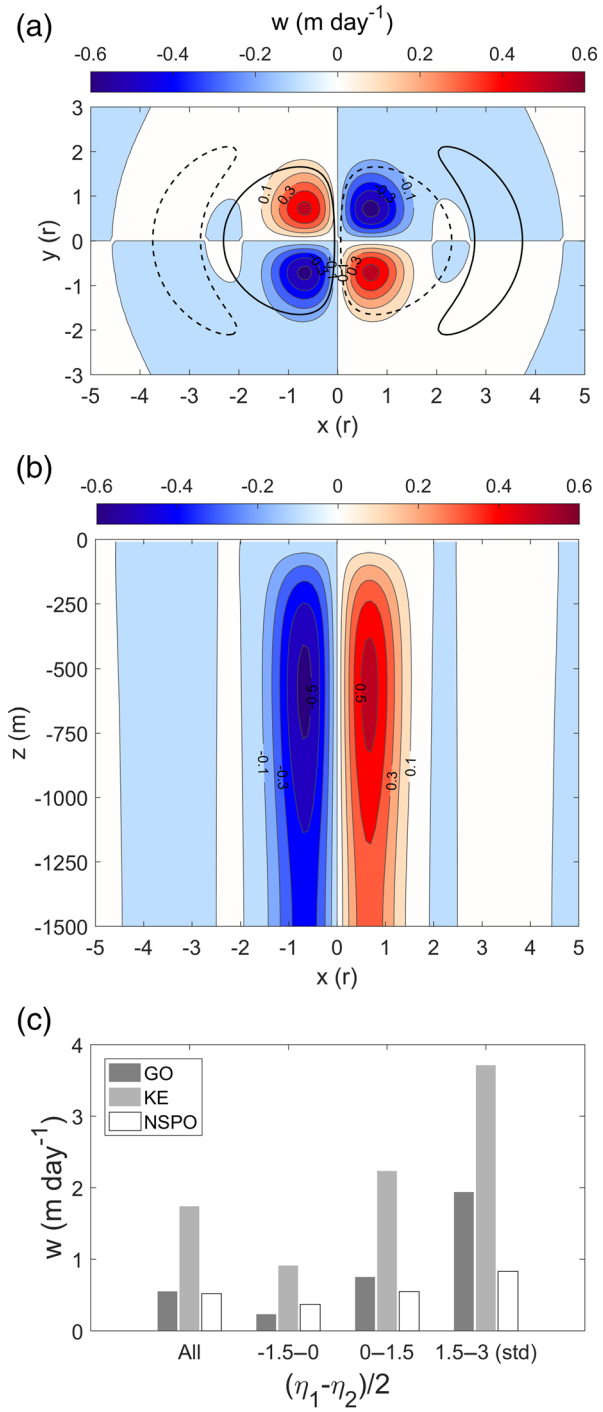

Figure 8. Frontogenetic vertical velocity (m day^{-1}) inside the reconstructed mesoscale dipole. (a) Horizontal pattern of w at 600 m depth. Black bold solid and dashed contours mark $P' = 0.1$ and $P' = -0.1$, respectively. (b) The same as Figure 8a but for the vertical section along $y = -0.7$. (c) Histogram of w maxima for dipoles in different regions and of different strength as measured by $\frac{\eta_1 - \eta_2}{2}$ (all, −1.5–0, 0–1.5, and 1.5–3 standard deviations [std] relative to the mean), where η_1 (η_2) is the SLA at the center of the anticyclonic (cyclonic) eddy. Here dipoles in the 1.5–3 std category are regarded as strong dipoles. GO, KE, and NSPO represent Global Ocean, Kuroshio Extension and Northwestern Subtropical Pacific Ocean, respectively.

when averaged only over the strong dipoles (Figure 8c). Large spatial variability is found in these vertical motions associated with mesoscale dipoles. For example, the Kuroshio Extension (140°–170°E, 30°–40°N) is a region of strong dipole-induced vertical velocities (±1.7 m day^{-1} when averaged over all the dipoles in this region and approximately ±4 m day^{-1} over the stronger ones), while the Northwestern Subtropical Pacific Ocean (125°–155°E, 15°–25°N) is a region of relatively weak dipole-induced vertical velocities (still around ±0.5 m day^{-1} when averaged over all the dipoles). In comparison, vertical motions achieved by the large-scale wind Ekman pumping are on the order of 0.1 m day^{-1}. Additional analysis confirms that the QG vertical velocities calculated from the composite or reconstructed dipole structure are very similar to the composite average of QG vertical velocities calculated from instantaneous dipole structures (Appendix A.3; Figure A3).

The dipole structure of mesoscale eddies leads to sharp fronts and strong currents between the two counterrotating eddies and also modifies their relative vorticity (Figure 7). Here we apply uniform winds of varying strength over a mesoscale dipole and two corresponding circular eddies, respectively, to examine the influence of the dipole structure on linear and nonlinear wind Ekman pumping over mesoscale eddies (Figure 9). The linear and nonlinear wind Ekman pumping velocities, w_{lin} and w_{non}, are calculated via (Gaube et al., 2015; Martin & Richards, 2001; McGillicuddy et al., 2007)

$$w_{lin} = \frac{1}{\rho_0(f+\xi)}\left(\frac{\partial \tau_y}{\partial x} - \frac{\partial \tau_x}{\partial y}\right),\ w_{non} = \frac{1}{\rho_0(f+\xi)^2}\left(\tau_x\frac{\partial \xi}{\partial y} - \tau_y\frac{\partial \xi}{\partial x}\right),$$

where $\xi = \frac{\partial v}{\partial x} - \frac{\partial u}{\partial y}$ is the relative vorticity associated with ocean surface currents and τ_x and τ_y are the x and y components of the surface (relative) wind stress. The linear wind Ekman pumping takes into account the relative wind effect, while the nonlinear wind Ekman pumping accounts for the relative vorticity of ocean surface currents (Gaube et al., 2015; Hughes & Wilson, 2008; McGillicuddy et al., 2007; Zhai et al., 2012).

The spatial pattern and magnitude of Ekman upwelling and downwelling in and around the dipole are sensitive to the direction of the applied wind forcing relative to the dipole orientation (Figures 9 and 10). Consider the idealized case of a down-jet wind where the wind and the jet between the dipole eddies are aligned. The linear wind Ekman pumping is upward in the anticyclonic eddy and downward in the cyclonic eddy, that is, acting to mechanically damp the dipole (Figure 9a). The nonlinear wind Ekman pumping, on the other hand, is strongly positive between the two dipole eddy centers, flanked by weaker downwelling on either side (Figure 9b). Comparing to the case of isolated circular eddies, the dipole structure enhances the magnitude of nonlinear wind Ekman pumping by about 50%, regardless of the strength of the applied wind forcing (Figure 9e).

Next we conduct composite analysis of w_{non} over detected mesoscale dipoles following Gaube et al. (2015). The large-scale background wind field is first estimated by spatially smoothing the daily

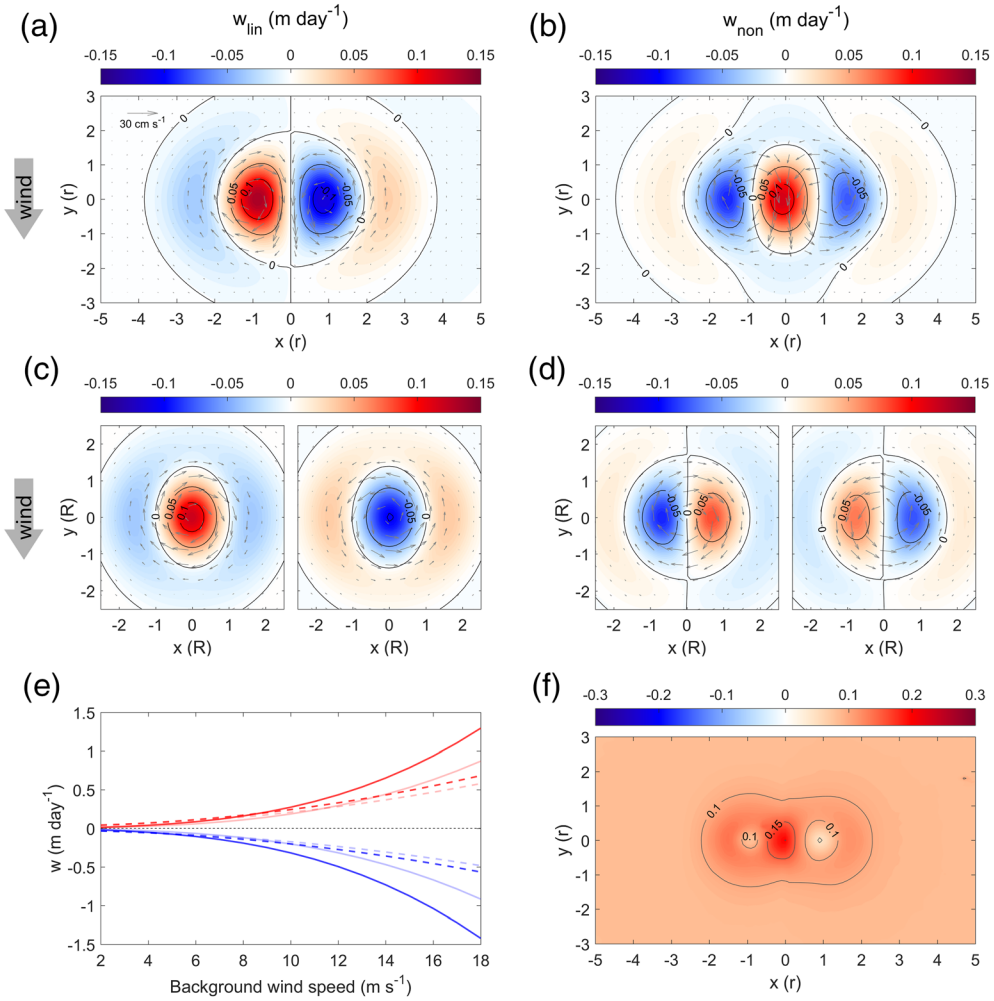

Figure 9. Linear and nonlinear Ekman pumping velocity (m day^{-1}) in the presence of dipoles and isolated circular eddies. (a, b) Horizontal patterns of the dipole-induced w_{lin} and w_{non} (color shading and contours) when subject to uniform down-jet winds of 7 m s^{-1}. Gray arrows indicate surface geostrophic currents. (c, d) The same with Figures 9a and 9b but for isolated circular eddies. (e) w_{lin} and w_{non} maxima (red) and minima (blue) as a function of the strength of the applied wind forcing. Dashed and solid curves correspond to w_{lin} and w_{non}, and dark- and light-color curves correspond to the dipoles and isolated circular eddies, respectively. (f) Composite average of absolute values of w_{non} in the dipole coordinate estimated from scatterometer winds and SLA-derived dipole surface geostrophic currents.

scatterometer vector winds to remove mesoscale wind variability with wavelength scales shorter than 6°. We then estimate w_{non} for each dipole pair by combining SLA-derived dipole geostrophic currents and collocated large-scale wind field. To isolate dipole-induced Ekman pumping, w_{non} is further spatially high pass-filtered with half-power cutoffs of 6° to remove the basin-scale Ekman pumping associated with the large-scale wind field. Finally, the absolute values of dipole-induced w_{non} are composite averaged onto the dipole coordinate. Figure 9f shows composite average of absolute values of w_{non} in the dipole coordinate, which confirms a similar percentage difference between values in the central jet area and those on the other flanks of the two dipole eddies as that in the idealized case (Figure 9b). It is worth pointing out that Ekman pumping associated with mesoscale dipoles is not a linear summation of those induced by the two corresponding circular eddies, since, by definition, there is considerable eddy deformation between the two dipole eddy centers which leads to an enhanced horizontal vorticity gradient there.

SST anomalies associated with ocean eddies can modify turbulence in the atmospheric boundary layer and thereby affect near-surface winds and other meteorological properties (Frenger et al., 2013; Gaube et al., 2015). Here we collocate satellite-derived SST and scatterometer wind stress anomalies over

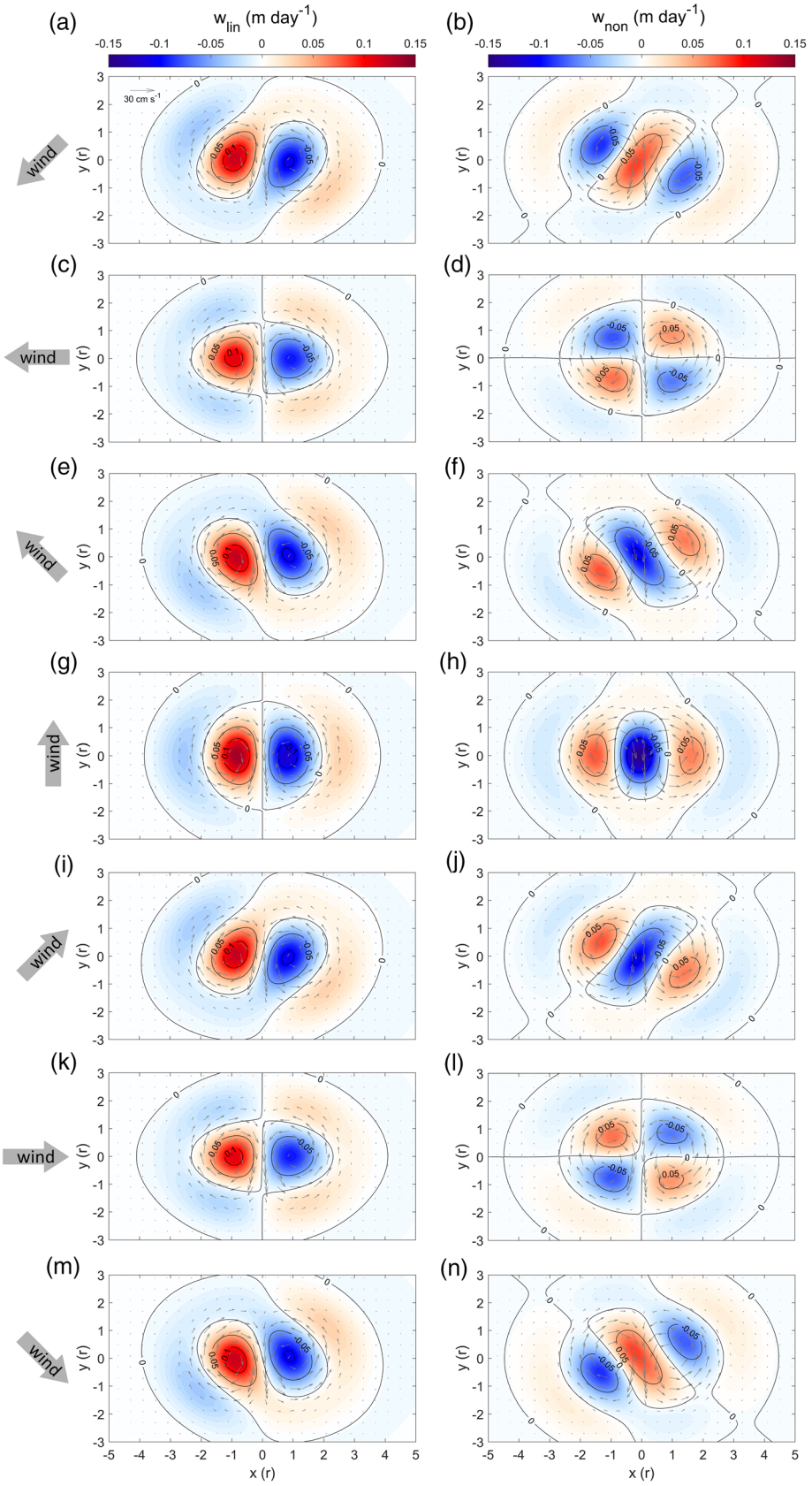

Figure 10. Same with Figures 9a and 9b but for winds from other directions.

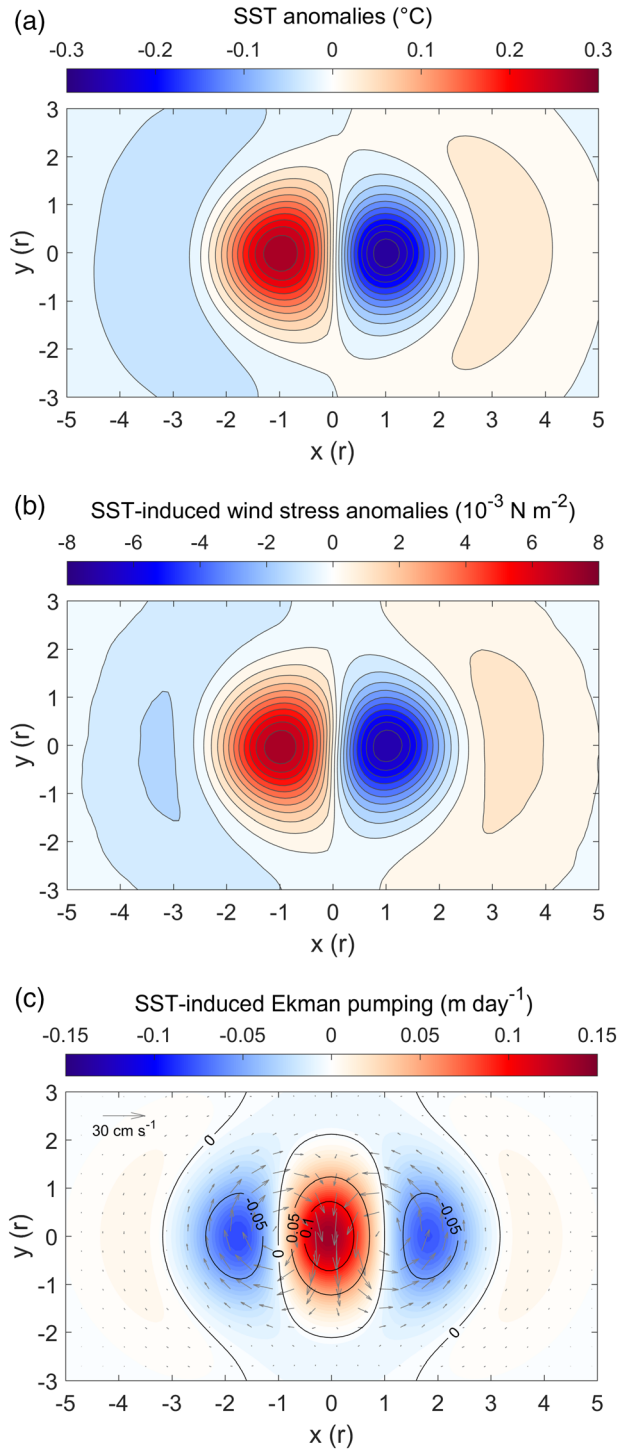

Figure 11. Dipole SST-induced wind stress and Ekman pumping anomalies. (a) Composite average of sea surface temperature anomalies (°C). Black contours correspond to 20 iso-contours of equal intervals. (b) Same with Figure 11a but for scatterometer wind stress anomalies (10^{-3} N m^{-2}). (c) Ekman pumping velocity (m day^{-1}) induced by wind stress anomalies shown in Figure 11b, assuming a down-jet background wind stress in the dipole coordinate.

detected mesoscale dipoles and compute their composite averages. The composite SST and wind stress magnitude anomalies show nearly identical dipole patterns and are positively correlated with each other, that is, stronger wind stress over positive SST anomaly (Figures 11a and 11b). This positive correlation indicates that it is the dipole-induced SST anomalies that lead to surface wind stress anomalies, not vice versa. Furthermore, the resemblance of dipole SST and wind stress magnitude anomalies points to downward momentum mixing as the underlying mechanism (Chelton & Xie, 2010; Frenger et al., 2013): Positive (negative) SST anomalies induce anomalous upward (downward) air-sea heat flux, which then strengthens (weakens) near-surface wind and wind stress by enhancing (reducing) turbulent mixing and downward momentum transport in the atmospheric boundary layer. Assuming a down-jet background wind stress in the dipole coordinate, the SST-induced wind stress anomalies result in a pattern of broad upwelling with a magnitude of over ± 0.1 m day^{-1} between the two dipole eddy centers, sandwiched by downwelling of half its strength on either side (Figure 11c).

4. Conclusions

In this study we have provided the first observational evidence to show that mesoscale dipoles are widespread features in the global ocean. These dipoles can lead to strong and deep-reaching vertical motions via frontogenesis and dipole-wind interaction. The vertical velocity induced by the dipole structure is comparable in magnitude with those associated with other mesoscale and even some submesoscale physical processes (Gaube et al., 2015; Klein & Lapeyre, 2009; Mahadevan, 2016; Pascual et al., 2015). Furthermore, frontogenesis and frontal-instability processes associated with mesoscale dipoles are likely to enhance submesoscale eddy generation (Capet et al., 2008; Klein & Lapeyre, 2009; Mahadevan, 2016). Given their abundance, mesoscale dipoles may play an important role in the Earth's biogeochemical processes via supplying nutrients to the surface ocean to support primary production and sequestering carbon to the deep ocean. Ocean models used for long-range climate simulations will rely on parameterizing the effect of mesoscale eddies for some time into the future. However, no existing eddy parameterization schemes explicitly account for tracer transports by mesoscale dipoles, a deficiency that needs to be resolved in the development of next generation of Earth system models.

Appendix A

A.1 Evolution of Composite Dipole in a Quasi-geostrophic Model

Here we initialize a quasi-geostrophic (QG) reduced gravity model on an *f* plane with the vorticity field associated with the composite dipole derived from altimeter data to see how it evolves with time in a medium that is at rest. The model potential vorticity is governed by

$$\frac{\partial q}{\partial t} + J(\psi, q) = 0,\ q = \nabla^2\psi - \frac{f^2}{g'H}\psi,$$

where q is the potential vorticity, J is the Jacobian operator, ψ is the stream function, f is the Coriolis parameter (at 25°N), $g' = 0.02$ m s^{-2} is the reduced gravity, and $H = 700$ m is the thickness of the upper layer. The Fourier spectral method is used to calculate spatial derivatives, and the fourth-order Runge-Kutta time stepping is used to integrate the model forward in time (Ni et al., 2020). The initial composite dipole is nonlinear, characterized by bulging in the y direction rather than circular in shape, and the dipole is flanked on each side by crescents of opposite sign vorticity. Consistent with Couder and Basdevant (1986), the external crescents initially slow down the two dipole eddies by compressing them against each other to form a linear dipole (Figures A1a–A1d). After that, the linear dipole, characterized by the circular shape of its vorticity field, translates at a much greater speed—four to five times the speed of the initial nonlinear dipole.

A.2 Errors and Uncertainties in Hydrostatic Integration

In this study, subsurface pressure anomalies are obtained by integrating the hydrostatic equation downward (Mulet et al., 2012) from the sea surface using AVISO SLA and Argo density anomalies. As an attempt to estimate errors associated with this calculation (combining two independently processed data sets in the hydrostatic integration), we process the high-resolution sea level output from the (1/12th)° HYCOM simulation in three different ways and generate three SLA products for the NSPO and KE regions. The first way is similar to the procedure used to produce the AVISO SLA product. After removing a multiyear mean from the

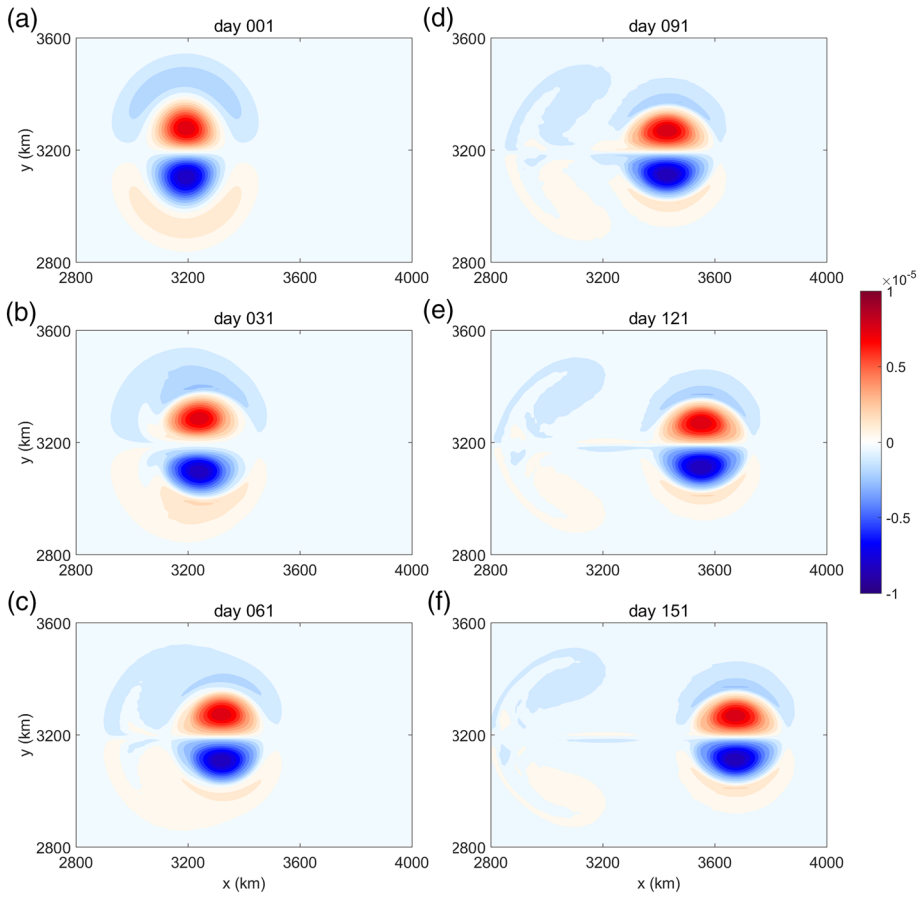

Figure A1. Dipole evolution in a quasi-geostrophic model on an f-plane, initiated with the vorticity field associated with the composite dipole derived from altimeter data. Color shading indicates relative vorticity (s^{-1}).

original HYCOM output, a band-pass Gaussian filter with half-power cutoff wavelengths between a latitude-dependent wavelength and 10° is applied to the daily SLA maps to isolate mesoscale signals. Following the AVISO procedure (Pujol et al., 2016), this latitude-dependent wavelength is set to be 1° and 0.6° for the NSPO and KE regions, respectively. Finally, these spatially filtered HYCOM SLA maps are

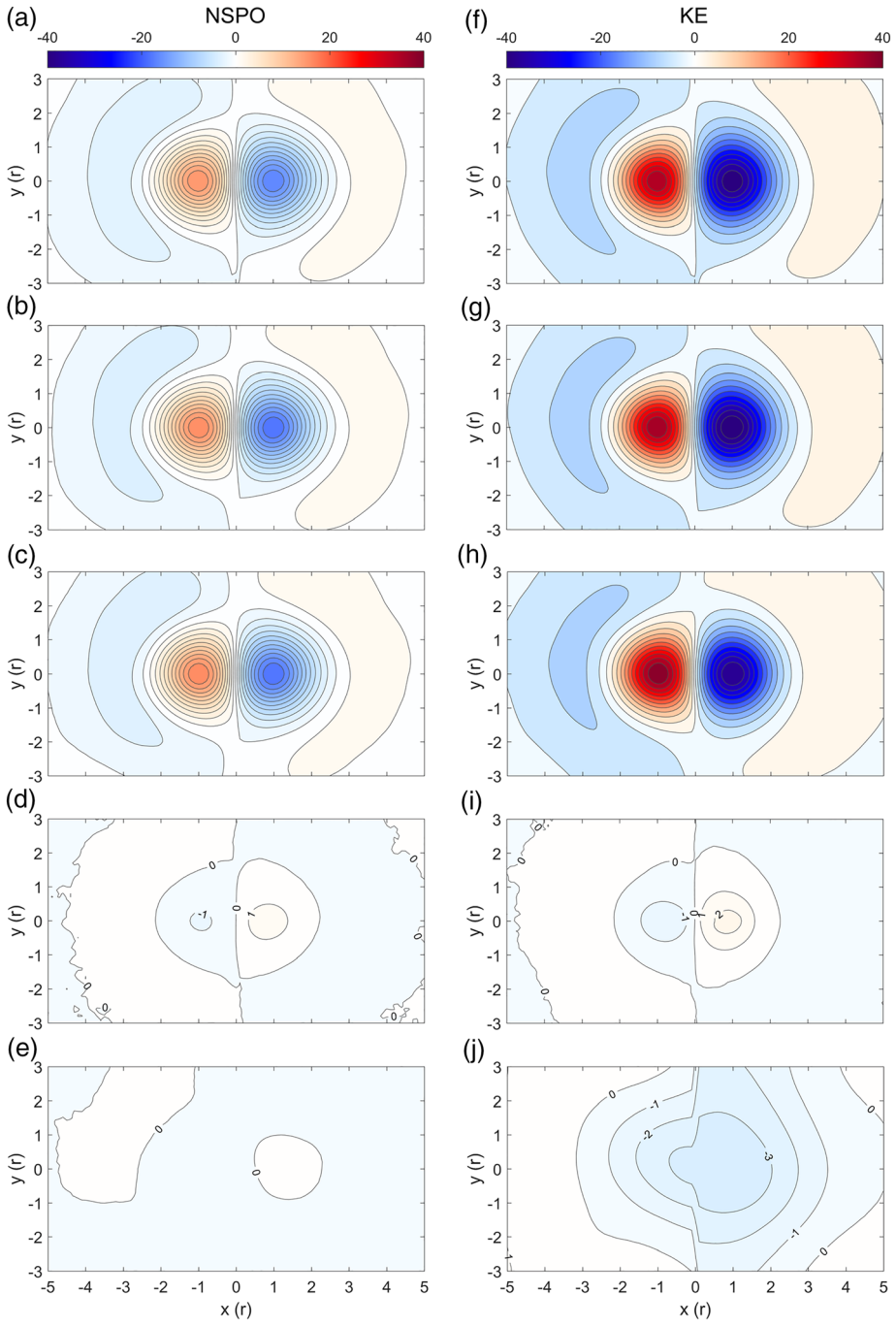

Figure A2. (a) Composite average of dipole SLA (cm) in the Northwestern Subtropical Pacific Ocean (NSPO) region from a HYCOM SLA product generated with a similar procedure as that used in the AVISO product. Black contours denote 20 iso-contours of equal intervals. (b) The same with Figure A2a but from a HYCOM SLA product that involves no coarse graining. (c) The same with Figure A2a but from a HYCOM SLA product generated in the same way as the Argo anomalies. (d) Difference between Figures A2a and A2b. (e) Difference between Figures A2b and A2c. (f–j) The same with Figures A2a–A2e but for the KE region.

subsampled onto the coarser AVISO grid (0.25° × 0.25°) to generate the first SLA product. In the second SLA product, we preserve eddy features resolved by the high-resolution HYCOM simulation by (1) applying a high-pass spatial filter with a half-power cutoff wavelength of 10° to the HYCOM SLA maps and (2) not subsampling the spatially filtered SLA maps onto the coarser AVISO grid. The third SLA product is generated in the same way as the Argo anomalies, where mesoscale SLAs are obtained by removing a local climatological mean. The local climatological mean is computed by averaging the original HYCOM output within a moving window of 5° × 5° (and within 45 days). Mesoscale dipoles identified from the three SLA products are then composite averaged and compared. It is found that processing the original HYCOM output in different ways (i.e., AVISO way and Argo way) leads to composite errors of less than 1.5 and 3.5 cm in NSPO and KE, respectively, corresponding to ~10% of the composite magnitude in both regions (Figure A2).

A.3 Errors and Uncertainties in QG Vertical Velocities

To assess the robustness of the QG vertical velocities, we compare dipole-induced vertical velocities calculated in different ways in the NSPO region, making use of the daily output from the (1/12th)° HYCOM simulation. In the first way, we composite average all the dipoles in the NSPO region and then calculate QG vertical velocities from the composite dipole structure (Figure A3a). In the second way, we calculate the daily QG vertical velocities for each dipole pair in this region, which include short-time and small-scale signals resolved by HYCOM, and then composite average them onto the dipole coordinate (Figure A3b). The dipole-induced vertical velocities calculated in these two different ways are very similar to each other, and both show a quadrupolar pattern of upwelling and downwelling with a magnitude of ~0.6 m day^{-1}. To further test the influence of spatial resolution on dipole-induced QG vertical velocities, we subsample the original (1/12th)° HYCOM output onto coarser grids (1/4° and 1/6°), calculate daily QG vertical velocities for each dipole pair using the coarse-grained model output, and then composite average them onto the

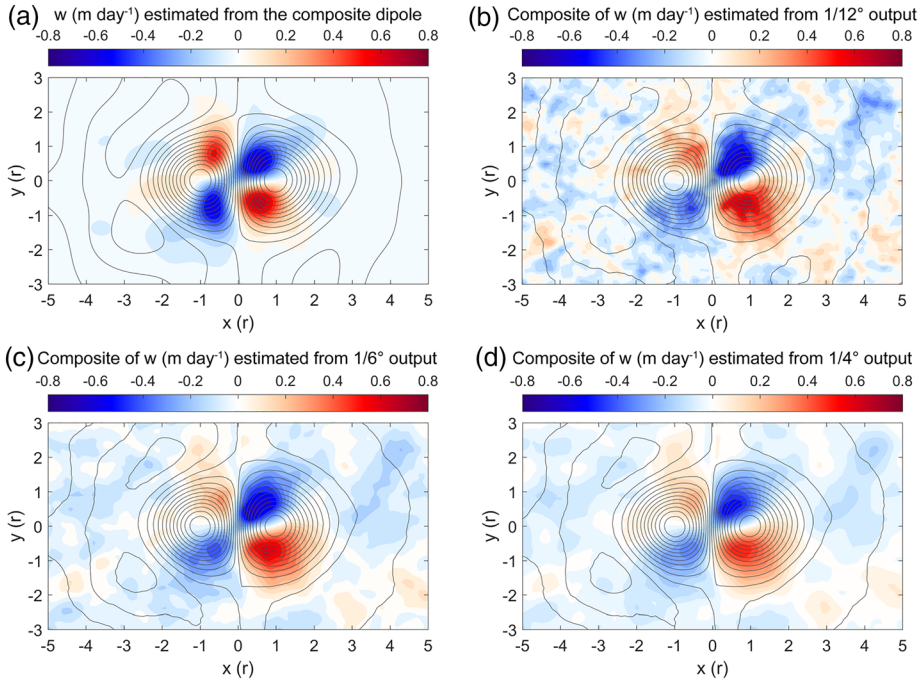

Figure A3. (a) QG vertical velocities calculated from the composite dipole structure in the NSPO region using output from the (1/12th)° HYCOM simulation over the period of 2005–2009. The color shading represents the vertical velocity (m day^{-1}), and black contours represent 20 iso-contours of the composite SLA with equal intervals. (b) Composite average of QG vertical velocities calculated from daily (1/12th)° HYCOM output in the same region and over the same period. (c) The same with Figure A3b but calculated from the daily HYCOM output subsampled onto the 1/6° grid. (d) The same with Figure A3b but calculated from the daily HYCOM output subsampled onto the 1/4° grid.

dipole coordinate (Figures A3c and A3d). The results show that the composite dipole QG vertical velocity is not overly sensitive to the spatial resolution used.

Data Availability Statement

The altimeter data are downloaded from Copernicus Marine Environment Monitoring Service (at http://marine.copernicus.eu/), the Argo float data are downloaded from the China Argo Real-time Data Center (at http://www.argo.org.cn), the microwave SST data are downloaded from Remote Sensing Systems (at http://www.remss.com/), the QuikSCAT scatterometer wind stress data are downloaded from IFREMER (at http://cersat.ifremer.fr/), and the high-resolution HYCOM simulation output is downloaded online (from https://hycom.org/).

Acknowledgments

Qinbiao Ni is supported by a visiting scholarship from the Chinese Scholarship Council and NSFC Grants 41811530301 and 41730535. Xiaoming Zhai acknowledges support by a Royal Society International Exchanges Award (IEC/NSFC/170007). Guihua Wang acknowledges support by NSFC Grants 42030405, 41576022 and 41976003 and National Key Research and Development Program of China (2019YFC1510100). Qinbiao Ni thanks Xuemin Jiang, Shenjie Zhou, Chi Xu, Zhibin Yang, Chuanyin Wang, and Enric Pallàs-Sanz for their helpful discussions. We thank the two reviewers for their constructive comments.

References

Ahlnäs, K., Royer, T. C., & George, T. H. (1987). Multiple dipole eddies in the Alaska Coastal Current detected with Landsat thematic mapper data. *Journal of Geophysical Research*, *92*(C12), 13,041–13,047. http://doi.org/10.1029/JC092iC12p13041

Batchelor, G. K. (1967). *An introduction to fluid dynamics*. Cambridge: Cambridge University Press. https://doi.org/10.1017/CBO9780511800955

Callendar, W., Klymak, J. M., & Foreman, M. G. G. (2011). Tidal generation of large sub-mesoscale eddy dipoles. *Ocean Science*, *7*(4), 487–502. http://doi.org/10.5194/os-7-487-2011

Capet, X., Mcwilliams, J. C., Molemaker, M. J., & Shchepetkin, A. F. (2008). Mesoscale to submesoscale transition in the California Current System. Part II: Frontal processes. *Journal of Physical Oceanography*, *38*(1), 44–64. http://doi.org/10.1175/2007JPO3672.1

Chaigneau, A., Texier, M. L., Eldin, G., Grados, C., & Pizarro, O. (2011). Vertical structure of mesoscale eddies in the eastern South Pacific Ocean: A composite analysis from altimetry and Argo profiling floats. *Journal of Geophysical Research*, *116*, C11025. http://doi.org/10.1029/2011JC007134

Chelton, D. B., Schlax, M. G., & Samelson, R. M. (2011). Global observations of nonlinear mesoscale eddies. *Progress in Oceanography*, *91*(2), 167–216. http://doi.org/10.1016/j.pocean.2011.01.002

Chelton, D. B., & Xie, S. P. (2010). Coupled ocean-atmosphere interaction at oceanic mesoscales. *Oceanography*, *23*(4), 52–69. http://doi.org/10.5670/oceanog.2010.05

Conway, T. M., Palter, J. B., & de Souza, G. F. (2018). Gulf Stream rings as a source of iron to the North Atlantic subtropical gyre. *Nature Geoscience*, *11*, 594–598. http://doi.org/10.1038/s41561-018-0162-0

Couder, Y., & Basdevant, C. (1986). Experimental and numerical study of vortex couples in two-dimensional flows. *Journal of Fluid Mechanics*, *173*, 225–251. http://doi.org/10.1017/S0022112086001155

de Ruijter, W. P. M., van Aken, H. M., Beier, E. J., Lutjeharms, J. R. E., Matano, R. P., & Schouten, M. W. (2004). Eddies and dipoles around south Madagascar: Formation, pathways and large-scale impact. *Deep Sea Research Part I*, *51*(3), 383–400. http://doi.org/10.1016/j.dsr.2003.10.011

Dong, C., Mcwilliams, J. C., Liu, Y., & Chen, D. (2014). Global heat and salt transports by eddy movement. *Nature Communications*, *5*, 3294. http://doi.org/10.1038/ncomms4294

Flierl, G. R., Larichev, V. D., McWilliams, J. C., & Reznik, G. M. (1980). The dynamics of baroclinic and barotropic solitary eddies. *Dynamics of Atmospheres and Oceans*, *5*(1), 1–41. http://doi.org/10.1016/0377-0265(80)90009-3

Flierl, G. R., Stern, M. E., & Whitehead, A. J. (1983). The physical significance of modons: Laboratory experiments and general integral constraints. *Dynamics of Atmospheres and Oceans*, *7*(4), 233–263. http://doi.org/10.1016/0377-0265(83)90007-6

Frenger, I., Gruber, N., Knutti, R., & Münnich, M. (2013). Imprint of Southern Ocean eddies on winds, clouds and rainfall. *Nature Geoscience*, *6*, 608–612. http://doi.org/10.1038/ngeo1863

Gaube, P., Chelton, D. B., Samelson, R. M., Schlax, M. G., & O'Neill, L. W. (2015). Satellite observations of mesoscale eddy-induced Ekman pumping. *Journal of Physical Oceanography*, *45*, 104–132. http://doi.org/10.1175/JPO-D-14-0032.1

Hesthaven, J. S., Lynov, J. P., Nielsen, A. H., Rasmussen, J. J., Schmidt, M. R., Shapiro, E. G., & Turitsyn, S. K. (1995). Dynamics of a nonlinear dipole vortex. *Physics of Fluids*, *7*(9), 2220–2229. http://doi.org/10.1063/1.868470

Hooker, S. B., Brown, J. W., Kirwan, A. D. Jr., Lindemann, G. L., & Mied, R. P. (1995). Kinematics of a warm-core dipole ring. *Journal of Geophysical Research*, *100*, 24,797–24,809. http://doi.org/10.1029/95JC02900

Hoskins, B. J., Draghici, I., & Davies, H. C. (1978). A new look at the ω-equation. *Quarterly Journal of the Royal Meteorological Society*, *104*(439), 31–38. http://doi.org/10.1002/qj.49710443903

Hughes, C. W., & Miller, P. I. (2017). Rapid water transport by long-lasting modon eddy pairs in the southern midlatitude oceans. *Geophysical Research Letters*, *44*, 12,375–12,384. http://doi.org/10.1002/2017GL075198

Hughes, C. W., & Wilson, C. (2008). Wind work on the geostrophic ocean circulation, including effects of small scales in the wind stress. *Journal of Geophysical Research*, *113*, C02016. http://doi.org/10.1029/2007JC004371

Klein, P., & Lapeyre, G. (2009). The oceanic vertical pump induced by mesoscale and submesoscale turbulence. *Annual Review of Marine Science*, *1*(1), 351–375. http://doi.org/10.1146/annurev.marine.010908.163704

Mahadevan, A. (2016). The impact of submesoscale physics on primary productivity of plankton. *Annual Review of Marine Science*, *8*, 161–184. http://doi.org/10.1146/annurev-marine-010814-015912

Martin, A. P., & Richards, K. J. (2001). Mechanisms for vertical nutrient transport within a North Atlantic mesoscale eddy. *Deep Sea Research Part II*, *48*(4–5), 757–773. http://doi.org/10.1016/S0967-0645(00)00096-5

McGillicuddy, D. J., Anderson, L. A., Bates, N. R., Bibby, T., Buesseler, K. O., Carlson, C. A., et al. (2007). Eddy/wind interactions stimulate extraordinary mid-ocean plankton blooms. *Science*, *316*(5827), 1021–1026. http://doi.org/10.1126/science.1136256

McWilliams, J. C., Flierl, G. R., Larichev, V. D., & Reznik, G. F. M. (1981). Numerical studies of barotropic modons. *Dynamics of Atmospheres and Oceans*, *5*(4), 219–238. https://doi.org/10.1016/0377-0265(81)90001-4

McWilliams, J. C., & Zabusky, N. J. (1982). Interactions of isolated vortices I: Modons colliding with modons. *Geophysical and Astrophysical Fluid Dynamics*, *19*, 207–227. http://doi.org/10.1080/03091928208208956

Mulet, S., Rio, M. H., Mignot, A., Guinehut, S., & Morrow, S. (2012). A new estimate of the global 3D geostrophic ocean circulation based on satellite data and in-situ measurements. *Deep Sea Research Part II*, *77–80*, 70–81. http://doi.org/10.1016/j.dsr2.2012.04.012

Ni, Q., Zhai, X., Wang, G., & Marshall, D. P. (2020). Random movement of mesoscale eddies in the global ocean. *Journal of Physical Oceanography*, *50*, 2341–2357. http://doi.org/10.1175/JPO-D-19-0192.1

Nikurashin, M., Vallis, G. K., & Adcroft, A. (2013). Routes to energy dissipation for geostrophic flows in the Southern Ocean. *Nature Geoscience*, *6*, 48–51. http://doi.org/10.1038/ngeo1657

Nycander, J. (1992). Refutation of stability proofs for dipole vortices. *Physics of Fluids*, *4*(3), 467–476. http://doi.org/10.1063/1.858319

Pallàs-Sanz, E., & Viúdez, A. (2007). Three-dimensional ageostrophic motion in mesoscale vortex dipoles. *Journal of Physical Oceanography*, *37*(1), 84–105. http://doi.org/10.1175/JPO2978.1

Pascual, A., Ruiz, S., Buongiorno Nardelli, B., Guinehut, S., Iudicone, D., & Tintoré, J. (2015). Net primary production in the Gulf Stream sustained by quasi-geostrophic vertical exchanges. *Geophysical Research Letters*, *42*, 441–449. http://doi.org/10.1002/2014GL062569

Penven, P., Echevin, V., Pasapera, J., Colas, F., & Tam, J. (2005). Average circulation, seasonal cycle, and mesoscale dynamics of the Peru Current System: A modeling approach. *Journal of Geophysical Research*, *110*, C10021. http://doi.org/10.1029/2005JC002945

Pidcock, R., Martin, A., Allen, J., Painter, S. C., & Smeed, D. (2013). The spatial variability of vertical velocity in an Iceland basin eddy dipole. *Deep Sea Research Part I*, *72*, 121–140. http://doi.org/10.1016/j.dsr.2012.10.008

Pujol, M. I., Faugère, Y., Taburet, G., Dupuy, S., Pelloquin, C., Ablain, M., & Picot, N. (2016). DUACS DT2014: The new multi-mission altimeter data set reprocessed over 20 years. *Ocean Science*, *12*(5), 1067–1090. http://doi.org/10.5194/os-12-1067-2016

Simpson, J. J., & Lynn, R. J. (1990). A mesoscale eddy dipole in the offshore California Current. *Journal of Geophysical Research*, *95*(C8), 13,009–13,022. http://doi.org/10.1029/JC095iC08p13009

Souza, J. M. A. C., de Boyer Montégut, C., Cabanes, C., & Klein, P. (2011). Estimation of the Agulhas ring impacts on meridional heat fluxes and transport using ARGO floats and satellite data. *Geophysical Research Letters*, *38*, L21602. http://doi.org/10.1029/2011GL049359

Wunsch, C. (1999). Where do ocean eddy heat fluxes matter? *Journal of Geophysical Research*, *104*, 13,235–13,249. http://doi.org/10.1029/1999JC900062

Xu, C., Zhai, X., & Shang, X. (2016). Work done by atmospheric winds on mesoscale ocean eddies. *Geophysical Research Letters*, *43*, 12,174–12,180. http://doi.org/10.1002/2016GL071275

Zhai, X., & Greatbatch, R. J. (2007). Wind work in a model of the northwest Atlantic Ocean. *Geophysical Research Letters*, *34*, L04606. http://doi.org/10.1029/2006GL028907

Zhai, X., Johnson, H. L., & Marshall, D. P. (2010). Significant sink of ocean-eddy energy near western boundaries. *Nature Geoscience*, *3*(9), 608–612. http://doi.org/10.1038/ngeo943

Zhai, X., Johnson, H. L., Marshall, D. P., & Wunsch, C. (2012). On the wind power input to the ocean general circulation. *Journal of Physical Oceanography*, *42*(8), 1357–1365. http://doi.org/10.1175/JPO-D-12-09.1

Zhang, Z., Wang, W., & Qiu, B. (2014). Oceanic mass transport by mesoscale eddies. *Science*, *345*, 322–324. http://doi.org/10.1126/science.1252418

Zhang, Z., Zhang, Y., & Wang, W. (2013). Universal structure of mesoscale eddies in the ocean. *Geophysical Research Letters*, *40*, 3677–3681. http://doi.org/10.1002/grl.50736